



# Magnetic Helicity from Multipolar Regions on the Solar Surface

PHILIPPE-A. BOURDIN<sup>1</sup>, , AXEL BRANDENBURG<sup>2,3,4,5</sup>, 

<sup>1</sup> Space Research Institute, Austrian Academy of Sciences, Schmiedlstr. 6, A-8042 Graz, Austria

<sup>2</sup> Nordita, KTH Royal Institute of Technology and Stockholm University, Roslagstullsbacken 23, SE-10691 Stockholm, Sweden

<sup>3</sup> JILA and Department of Astrophysical and Planetary Sciences, University of Colorado, Boulder, CO 80303, USA

<sup>4</sup> Department of Astronomy, AlbaNova University Center, Stockholm University, SE-10691 Stockholm, Sweden and

<sup>5</sup> Laboratory for Atmospheric and Space Physics, University of Colorado, Boulder, CO 80303, USA

Received 2018 April 11; revised 2018 October 12; accepted 2018 October 15; published 2018 December 5

## Abstract

The emergence of dipolar magnetic features on the solar surface is an idealization. Most of the magnetic flux emergence occurs in complex multipolar regions. Here, we show that the surface pattern of magnetic structures alone can reveal the sign of the underlying magnetic helicity in the nearly force-free coronal regions above. The sign of the magnetic helicity can be predicted to good accuracy by considering the three-dimensional position vectors of three spots on the sphere ordered by their relative strengths at the surface and compute from them the skew product. This product, which is a pseudoscalar, is shown to be a good proxy for the sign of the coronal magnetic helicity.

**Keywords:** Sun: magnetic fields — Sun: corona — dynamo — magnetohydrodynamics (MHD) — turbulence — methods: numerical

## 1. Introduction

The Sun’s magnetic field manifests itself through sunspots in white light and magnetograms in polarized light. The resulting pattern is generally rather complex and never in the form of a symmetric pair of spots that is usually shown in text books; see, e.g., Parker (1979). Just like a human face, both halves are never perfectly identical to their actual mirror images. In fact, certain aspects of the solar surface pattern are distinctly different from each other in the northern and southern hemispheres. This aspect has been explored by Sara Martin (1998a,b, 2003) and others (Canfield et al. 1999; Magara & Longcope 2001; Gibson et al. 2002); see also Panasenco & Martin (2008) and Panasenco et al. (2011, 2013) for recent accounts of those studies.

The purpose of this paper is to propose a simple recipe by which a pseudoscalar can be constructed that can be used to estimate the sign of the underlying magnetic helicity that is responsible for creating the surface magnetic field. To appreciate the motivation behind this way of thinking, we must recall that a pseudoscalar is a rather special type of mathematical construct. If one finds a way of constructing such a quantity from some physical object, it changes its sign when constructing it from a mirror image of the same object. A common example is the cyclones on the Earth’s weather map that look different from their mirror images. Mathematically, a pseudoscalar can be constructed from the downward direction given by the gravity vector  $\mathbf{g}$  and the local angular velocity vector  $\mathbf{\Omega}$ , which is an axial vector. If one draws this vector by indicating the sense of rotation rather than through an arrow on one of the two ends, it is evident that viewing it in a mirror results in the opposite sense of rotation. Therefore, the sign of the dot product  $\mathbf{g} \cdot \mathbf{\Omega}$  changes. It is therefore a pseudoscalar. In the Earth and in the Sun, it is this pseudoscalar that governs the sign of several other relevant pseudoscalars such as the kinetic, magnetic, and current helicities; see Brandenburg & Subramanian (2005) for a review.

One may now speculate that the construction of any pseudoscalar in a system must be related to some other pseudoscalar in that system, even though the causal relationship may not immediately be evident. Consider now a seemingly absurd looking example of a pseudoscalar,

$$Q = (\hat{\mathbf{n}}_1 \times \hat{\mathbf{n}}_2) \cdot \hat{\mathbf{n}}_3, \quad (1)$$

constructed from the normalized position vectors  $\hat{\mathbf{n}}_1$ ,  $\hat{\mathbf{n}}_2$ , and  $\hat{\mathbf{n}}_3$  of three different spots on the solar surface. In this definition,  $Q$  is independent of the sphere radius. Their unsigned fluxes are  $|\Phi_1|$ ,  $|\Phi_2|$ , and  $|\Phi_3|$ , and they are ordered such that  $|\Phi_1| < |\Phi_2| < |\Phi_3|$ .

Remarkably, the direction of the magnetic field does not enter, and we do not even need a vector-magnetogram. All that is required is any three spots that can somehow be ordered, for example, by their strength, as explained above.

In this paper, we test the idea outlined above by considering synthetic line-of-sight magnetograms and constructing from those a nearly force-free magnetic field in the corona on top of it. Such a magnetic field is in general always helical, so we can compute the sign of the magnetic helicity and compare it with the sign of  $Q$ . The idea of constructing a pseudoscalar  $Q$  from the position vectors of individual sources is not new and has been applied to the arrival directions of energetic GeV photons coming from extragalactic sources in the sky (Tashiro et al. 2014; Chen et al. 2015; Tashiro & Vachaspati 2015, who find evidence for a negative sign throughout all of the sky, which they associated with the possibility of a helical primordial magnetic field with negative helicity in all of the Universe). In their case, the arrival directions of GeV  $\gamma$ -rays in the sky is the result of magnetic deflection of pair-created particles resulting from the interaction of TeV photons from blazars with the extragalactic background light. In the present case, the location of spots on the solar or stellar surface is a more direct consequence of a dynamo-generated magnetic field somewhere beneath the surface (Brandenburg 2005).

In the solar corona, a force-free magnetic field can be constructed using a potential field extrapolation method. Only the line-of-sight magnetic field  $B_z(x, y)$  at the bottom boundary is needed. No magnetic helicity can readily be

arXiv:1804.04160v2 [astro-ph.SR] 8 Dec 2018

constructed from this, and yet a certain sign of the resulting magnetic helicity is somehow encoded in the photospheric magnetic pattern, provided it looks different from its mirror image, as alluded to above. This is indeed what was found in the recent work of Bourdin et al. (2018), using data from simulations of Bourdin et al. (2013).

Any distribution of  $B_z(x, y, z_*, 0)$  at the surface  $z = z_*$  can be used to construct a potential field  $\mathbf{B} = \nabla\varphi$ , where  $\varphi(x, y, z)$  obeys  $B_z(x, y, z_*, 0) = \partial\varphi/\partial z$  at  $z = z_*$ . At later times, however,  $B_z(x, y, z_*, t)$  changes on the boundary as the magnetic field patches expand due to diffusive and dynamical processes. The field then evolves through a sequence of new nonpotential nearly force-free states, with the current density being parallel to the magnetic field, which implies local current helicity.

The purpose of this work is to study the connection between the original orientation of spots, as characterized by the pseudoscalar  $Q$ , and the sign of the resulting magnetic helicity in the volume above. For this purpose, we solve for the magnetic field numerically using ambipolar diffusion as a relaxation method to construct approximately force-free magnetic fields above three- and four-spot arrangements as the lower boundary condition.

## 2. Method

### 2.1. Ambipolar relaxation approach

To construct an approximately force-free equilibrium magnetic field  $\mathbf{B}$ , one often uses the magnetofrictional approach (Yang et al. 1986), which corresponds to solving the induction equation with a velocity that is proportional to the Lorentz force,  $\mathbf{J} \times \mathbf{B}$ , where  $\mathbf{J} = \nabla \times \mathbf{B}/\mu_0$  is the current density and  $\mu_0$  is the vacuum permeability. One usually divides this velocity by  $\mathbf{B}^2$  to enhance the relaxation rate in regions of weak magnetic field (Valori et al. 2007), but this is purposely ignored here, so our effective advection velocity is  $\mathbf{v} = (\tau/\rho)\mathbf{J} \times \mathbf{B}$ , where  $\tau$  is some relaxation time and  $\rho$  is some density, which is assumed constant. Inserting this into the induction equation, the electromotive force  $\mathbf{v} \times \mathbf{B}$  becomes proportional to  $(\mathbf{J} \times \mathbf{B}) \times \mathbf{B} = (\mathbf{J} \cdot \mathbf{B})\mathbf{B} - \mathbf{B}^2\mathbf{J}$ , so the uncurled evolution equation for the magnetic vector potential  $\mathbf{A}$ , where  $\mathbf{B} = \nabla \times \mathbf{A}$ , can be written as

$$\frac{\partial \mathbf{A}}{\partial t} = \alpha_{\text{AD}}\mathbf{B} - (\eta_{\text{AD}} + \eta)\mu_0\mathbf{J}, \quad (2)$$

where  $\alpha_{\text{AD}} = (\tau/\rho)(\mathbf{J} \cdot \mathbf{B})$  is a term reminiscent of the  $\alpha$  effect in mean-field electrodynamics (Krause & Rädler 1980),  $\eta_{\text{AD}} = (\tau/\rho)\mathbf{B}^2$  is an effective magnetic diffusivity that is what gives ambipolar diffusion its name,  $\eta$  is the usual Spitzer diffusivity, and the Weyl gauge has been adopted in Equation (2). Ambipolar diffusion is known to lead to the formation of sharp structures such as current sheets between nearly force-free regions in space (Brandenburg & Zweibel 1994). This is an important feature that appears more pronounced here than in the magnetofrictional approach, which motivates our choice of employing ambipolar diffusion.

To formulate the potential field boundary condition, we employ the Fourier-transformed magnetic vector potential

$$\tilde{\mathbf{A}}(k_x, k_y, z, t) = \int \mathbf{A}(x, y, z, t) e^{i\mathbf{k} \cdot \mathbf{r}} d^2\mathbf{r}, \quad (3)$$

where  $\mathbf{k} = (k_x, k_y)$  and  $\mathbf{r} = (x, y)$ . On the lower and upper

$z$  boundaries, we thus have

$$\frac{\partial \tilde{\mathbf{A}}}{\partial z} = -|\mathbf{k}|\tilde{\mathbf{A}}(k_x, k_y, z_*, t), \quad (4)$$

where  $z_*$  denotes the locations of the boundaries. One of them is the lower surface, which we will from now on assume to be at  $z = 0$ , and the other is at the top of the domain. Note that on both boundaries we assume the field to fall off with increasing values of  $z$ , which is not the standard situation on the lower boundary, if the region beneath it was supposed to be a vacuum. It is, however, a natural choice in the present context where the magnetic field is assumed to be initially potential inside the computational domain (Bourdin et al. 2013).

We use this formulation to set the Fourier-transformed magnetic vector potential in the ghost zones just outside the computational domain. This corresponds to setting boundary conditions for the derivative of all three components of  $\tilde{\mathbf{A}}$ , as stated above. We solve Equation (2) numerically using the PENCIL CODE<sup>1</sup> using a resolution of  $64^3$  meshpoints. The total vertical magnetic flux is always zero since  $\mathbf{A}$  is periodic in  $x$  and  $y$ , and we balance out  $B_z$  at the bottom.

### 2.2. Gauge-independent magnetic helicity

To characterize the magnetic helicity in a gauge-independent fashion, we use the formulation of Finn & Antonsen, Jr. (1985); see their Equation (5), which is identical to the relative helicity of Berger & Field (1984), and apply it to the semi-infinite test volume  $V(z)$ ;

$$H_{\text{M}}(z) = \iiint_z^\infty (\mathbf{A} + \mathbf{A}_{\text{pot}}) \cdot (\mathbf{B} - \mathbf{B}_{\text{pot}}) dz dy dx. \quad (5)$$

We use a potential field extrapolation from the vertical magnetic field  $B_z$  at the base of this test volume  $V$  as a reference field,  $\mathbf{B}_{\text{pot}} = \nabla \times \mathbf{A}_{\text{pot}}$ . Computing the helicity difference between two test volumes above heights  $z$  and  $z + \Delta z$ , we obtain the gauge-independent magnetic helicity contained in small horizontal slices of thickness  $\Delta z$  as

$$\Delta H_{\text{M}}(z; \Delta z) = H_{\text{M}}(z) - H_{\text{M}}(z + \Delta z). \quad (6)$$

Here, we simply use the grid distance of our simulation as  $\Delta z = 2\pi/64$ . We stop the integration at the upper boundary of our simulation domain, where the magnetic field is almost potential, so that the error we make in our limited integration is negligible. As required by Finn & Antonsen, Jr. (1985), the magnetic fields normal to the boundaries of the integration volume are identical. Because our setup is periodic in the horizontal directions, all assumptions on the boundaries of  $V$  apply only to the boundaries in  $z$ .

### 2.3. Arrangement of spots of different strengths

We consider configurations of  $N$  spots of different strengths  $|\Phi_1| < |\Phi_2| < \dots < |\Phi_N|$  as

$$B_z(x, y, z_0, t) = \sum_{\lambda=1}^N \Phi_\lambda e^{-(\mathbf{r}-\mathbf{r}_\lambda)^2/2\sigma^2} / (2\pi\sigma^2), \quad (7)$$

where  $\mathbf{r}_\lambda$  are the positions of the spots with magnetic fluxes  $\Phi_\lambda$  for  $\lambda = 1, 2, \dots, N$ , where  $N = 3$  in this case.

<sup>1</sup> <https://github.com/pencil-code>

**Table 1**Triangular cases with multiples of  $\Phi_0$  at the positions  $(r_1, r_2, r_3)$ 

#	$\Phi$	$Q/\ell^2$	$H_{6M+}$	$H_{6M-}$	$H_{C+}$	$H_{C-}$
A	(3, -1, -2)	+1	$\uparrow +3.17$	-2.22	+0.39	-35.0
A'	(-1, 3, -2)	-1	+2.22	$\uparrow -3.17$	+35.0	-0.39
$\mathcal{A}$	(3, 1, 2)	+1	$\uparrow +10.2$	-0.23	+1.36	-3.18
$\mathcal{A}'$	(1, 3, 2)	-1	+0.23	$\uparrow -10.2$	+3.18	-1.36
B	(-1, -2, 3)	+1	+0.17	-8.99	+0.07	-10.9
B'	(-2, -1, 3)	-1	+8.99	-0.17	+10.9	-0.07
$\mathcal{B}$	(1, 2, 3)	+1	+0.30	-3.68	$\downarrow +4.46$	-0.01
$\mathcal{B}'$	(2, 1, 3)	-1	+3.68	-0.30	+0.01	$\downarrow -4.46$
C	(-2, 3, -1)	+1	+0.00	-31.8	+8.78	-15.0
C'	(3, -2, -1)	-1	+31.8	-0.00	+15.0	-8.78
$\mathcal{C}$	(2, 3, 1)	+1	+0.00	-5.68	+0.70	-3.88
$\mathcal{C}'$	(3, 2, 1)	-1	+5.68	-0.00	+3.88	-0.70

Some numbers are displayed in italics to indicate a systematic trend.

We construct observables from spherical polar coordinates  $(r, \theta, \phi)$  at the surface as

$$\hat{\mathbf{n}} = (\sin \theta \cos \phi, \sin \theta \sin \phi, \cos \theta). \quad (8)$$

To map the corners of a triangle onto the sphere, we choose two neighboring unit vectors  $\hat{\mathbf{e}}_1$  and  $\hat{\mathbf{e}}_2$  on the sphere to define a local coordinate system spanned by the unit vectors  $\hat{\boldsymbol{\xi}}$  and  $\hat{\boldsymbol{\eta}}$  given by  $\boldsymbol{\xi} = \hat{\mathbf{e}}_2 - \hat{\mathbf{e}}_1$  and  $\boldsymbol{\eta} = \boldsymbol{\xi} \times \hat{\mathbf{e}}_1$ . Thus,

$$\hat{\mathbf{n}}_\lambda = \hat{\mathbf{e}}_1 + \mathbf{M}\hat{\mathbf{r}}_\lambda \quad \text{for } \lambda = 1, \dots, N, \quad (9)$$

where  $\mathbf{M} = (\hat{\boldsymbol{\xi}}, \hat{\boldsymbol{\eta}})$  is a  $2 \times 3$  matrix consisting of the two column vectors  $\hat{\boldsymbol{\xi}}$  and  $\hat{\boldsymbol{\eta}}$ . In practice, we take  $\hat{\mathbf{e}}_1 = (1, 0, 0)$  and  $\hat{\mathbf{e}}_2 = (\sin 30^\circ, \cos 30^\circ, 0)$ . The matrix  $\mathbf{M}$  describes the conversion of planar two-dimensional position vectors  $\mathbf{r}_\lambda$  onto the position vector  $\hat{\mathbf{n}}_\lambda$  on the unit sphere. In this formulation, position differences  $\mathbf{r}_\lambda - \mathbf{r}_{\lambda'}$  are then measured in radian. To obtain the corresponding values in degrees, we multiply by  $180^\circ/\pi$ .

#### 2.4. Three-spot arrangements

We begin with a triangular configuration with positions

$$\mathbf{r}_1 = (\ell, 0), \quad \mathbf{r}_2 = (0, \ell), \quad \mathbf{r}_3 = (\ell, \ell) \quad (\text{A-C}), \quad (10)$$

with indices (1, 2, 3) corresponding to spots of strengths  $\Phi_1/\Phi_0 = 1$ ,  $\Phi_2/\Phi_0 = 2$ , and  $\Phi_3/\Phi_0 = -3$ , where  $\Phi_0$  is another constant and  $\ell$  is the spot separation. This particular choice for the three values of  $|\Phi_\lambda|$  ensures vertical magnetic flux balance, although this is not actually required, as will be shown further below. We associate the positions  $(\mathbf{r}_1, \mathbf{r}_2, \mathbf{r}_3)$  with different permutations of the fluxes  $(\Phi_1, \Phi_2, \Phi_3)$ ; see Table 1.

The three spots, referred to as cases A–C in Equation (10), are arranged in a mathematically positive (counterclockwise) sense around their center of mass. The same three-spot arrangement, but with only positive polarities, will be referred to as cases  $\mathcal{A}$ – $\mathcal{C}$ .

In Table 1, we compare the sign of  $Q$  with the gauge-independent magnetic helicity; left-handed systems (L) have a positive  $Q$  value and generate negative helicity signs. We show the total magnetic (M) and current (C) helicities, where we sum separately the positive (+) and negative (–) parts in our domain that we compute as

$$\begin{aligned} H_{M\pm} &= \sum_{z|\Delta H_M(z) \geq 0} \Delta H_M(z), \\ H_{C\pm} &= \sum_{z|\Delta H_C(z) \geq 0} \Delta H_C(z), \end{aligned} \quad (11)$$

with  $\Delta H_C(z)$  being the total current helicity contained in the horizontal slice of volume  $4\pi^2\Delta z$ . In the tables, we give normalized values as  $H_{6M\pm} \equiv 10^6 H_{M\pm}$ . The total helicities of the whole domain may be obtained by summing the negative and positive helicities:

$$\begin{aligned} H_M &= H_{M+} + H_{M-}, \\ H_C &= H_{C+} + H_{C-}. \end{aligned} \quad (12)$$

Magnetic helicity values from the upper part of the domain are denoted by  $\uparrow$ . The current helicity values denoted with  $\downarrow$  are strongly influenced by the lower boundary and are therefore disregarded.

It turns out that the value of  $Q$  is proportional to  $\ell^2$ . In particular, for the triangular arrangement of the spots given by Equation (10), we have  $Q = \pm\ell^2$  for positive (negative) permutations of the spot's fluxes  $(\Phi_1, \Phi_2, \Phi_3)$ . Conversely, for a flipped arrangement of spots (A'–C'), we also find—not surprisingly—a flipped sign of  $Q$ . These three spots are now arranged in a mathematically negative sense around their center of mass.

Numerically, we find that for large values of  $\ell$ , corresponding to angular separations of spots in excess of  $20^\circ$ , the ratio  $|Q|/\ell^2$  drops significantly below unity. In general,  $Q/\ell^2$  is twice the area of the triangle spanned by the three points, so, by comparison, for a configuration consisting of an equilateral triangle, we have  $Q/\ell^2 = \pm \sin 60^\circ$  for spots of increasing strength in the positive (negative) mathematical sense.

In Figure 1, we show visualizations of  $B_z$ ,  $|\mathbf{J}|$ , and  $\mathbf{J} \cdot \mathbf{B}$  at the bottom surface. We recall that the configurations A and A', B and B', as well as C and C', each have opposite signs of current helicity. We confirmed that the polarities of the different patches is not important for the sign of the current helicity, but it is instead for the orientation of spots of increasing strength. In the visualizations of  $B_z$ , patches of increasing strengths are arranged in a clockwise sense, while those of A'–C' are in a counterclockwise sense. Comparing A–C with A'–C', we see that the current sheets are flipped about the diagonal, which is indicated by a long-dashed line.

The images of  $\mathbf{J} \cdot \mathbf{B}$  look more complex than those of  $B_z$  and  $|\mathbf{J}|$  because patches of opposite sign are now much smaller than the patches of  $B_z$ . However, one sees clearly that one is a mirror image of the other after a sign flip of  $\mathbf{J} \cdot \mathbf{B}$ . Apart from this, there is no change in the relative dominance of one sign relative to the other, and one would not be able to tell the sign of the  $xy$  averages  $(\mathbf{J} \cdot \mathbf{B})_{xy}$  judging just based on the sign of the local patches of  $\mathbf{J} \cdot \mathbf{B}$ . This demonstrates that what really matters in the end are both the sign of  $Q$  and the values of the unsigned flux of all spots, which is only obtained after averaging over all the patches.

Remarkably, as alluded to above, the sign of the polarities is not important for generating helicity. In cases  $\mathcal{A}$ – $\mathcal{C}$ , where all spots have the same polarity, we see that they also generate magnetic and current helicities, but less strongly so than compared to the arrangements A–C that have different signs in their polarities; see Figure 2. The current densities of the unipolar cases  $\mathcal{A}$ – $\mathcal{C}$  are of course stronger on the outer contour of the three-spot region. The angles between  $\mathbf{J}$  and  $\mathbf{B}$  have a less complex pattern. This is expected because of the less complex magnetic topology in the unipolar regions.

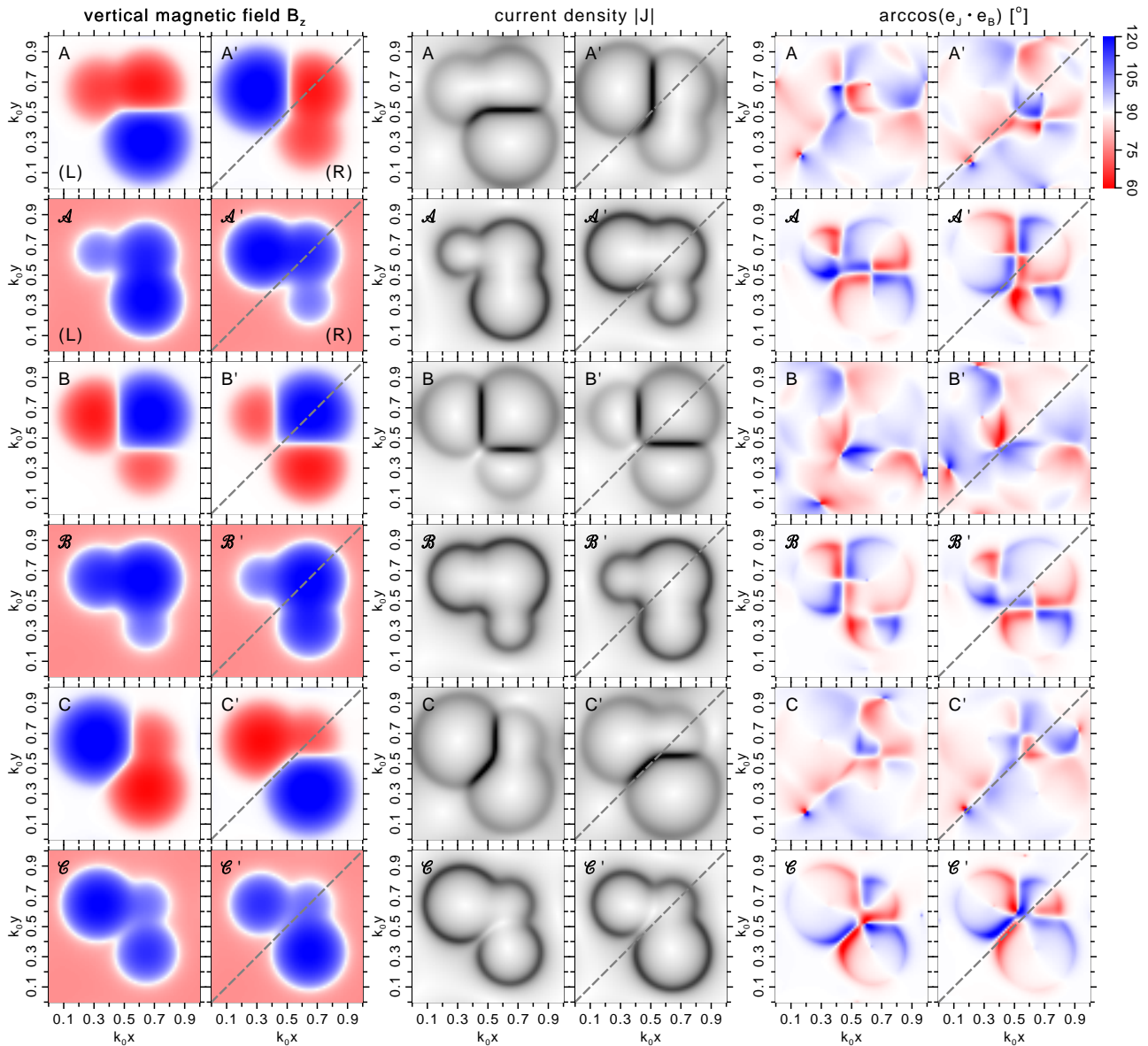


**Figure 1.** Overview of  $B_z(x,t)$  (red:  $B_z < 0$ , blue:  $B_z > 0$ ), current density (linear grayscale), and  $(\mathbf{J} \cdot \mathbf{B})_{xy}$  at an evolved snapshot at  $t = 7$  time units at the bottom boundary. The gray dashed line indicates the symmetry axis between cases  $X$  and  $X'$ ; see also Table 1. The letters L and R in the panels of  $|B_z|$  refer to left and right hands, respectively. The handedness is L in all panels  $X$  and R for all  $X'$ ; see Section 2.6.

### 2.5. Four-spot arrangements

In an attempt to generalize our approach to multiple spots, we now also consider four-spot arrangements with

$$\mathbf{r}_1 = (0, 0), \quad \mathbf{r}_2 = (\ell, 0), \quad \mathbf{r}_3 = (\ell, \ell), \quad \mathbf{r}_4 = (0, \ell), \quad (13)$$

which are referred to as cases D–F'; see Table 2. Each configuration is denoted by the vector

$$\Phi = (\Phi_a, \Phi_b, \Phi_c, \Phi_d) \quad (14)$$

for each of the positions  $(\mathbf{r}_1, \mathbf{r}_2, \mathbf{r}_3, \mathbf{r}_4)$ , being certain permutations of  $(\Phi_1, \Phi_2, \Phi_3, \Phi_4)$ , where the four fluxes obey  $|\Phi_1| < |\Phi_2| < |\Phi_3| < |\Phi_4|$ .

A four-spot arrangement can be analyzed by breaking it down into four different three-spot arrangements and calculating the weighted sum

$$S = \sum_{i=1}^4 q_i \phi_i, \quad (15)$$

**Table 2**

Quadratic cases with multiples of  $\Phi_0$  at the positions  $(r_1, r_2, r_3, r_4)$ .

#	$\Phi$	$S$	$H_{6M+}$	$H_{6M-}$	$H_{C+}$	$H_{C-}$
D	(0.5, 1.0, 1.5, -3)	+18	+8.70	-1.14	+31.0	-0.35
E	(0.5, 1.0, -3, 1.5)	-3	+0.18	-6.80	+0.08	-12.9
F	(0.5, 1.5, 1.0, -3)	+1	+1.10	↑ -3.01	+14.4	-0.86
E'	(0.5, 1.5, -3, 1.0)	+3	+6.80	-0.18	+12.9	-0.08
F'	(0.5, -3, 1.0, 1.5)	-1	↑ +3.01	-1.10	+0.86	-14.4

Some numbers are displayed in italics to indicate a systematic trend.

where  $q_i = Q_i/\ell^2 = \pm 1$  is the normalized  $Q$  value for triangle  $i$  and  $\phi_i$  is the total unsigned flux of each triangle, i.e.,

$$\phi = \sum_{\lambda=a}^c |\Phi_\lambda|, \quad (16)$$

which is different for each of the four triangles. In Ta-

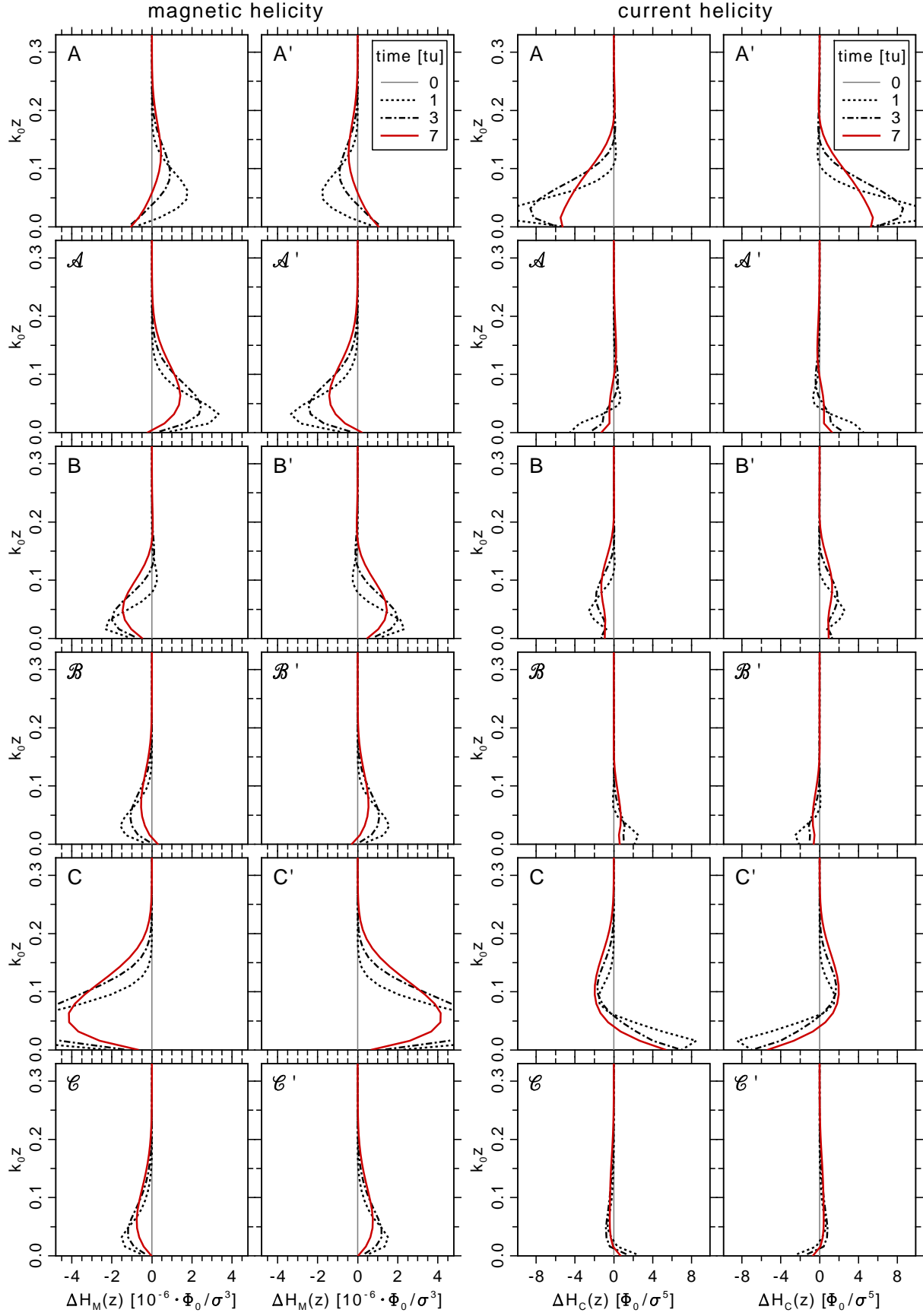


**Figure 2.** Overview of the magnetic and current helicity evolution for the signed and unsigned three-spot configurations as listed in Table 1 at three times. Time is given in arbitrary time units [tu].

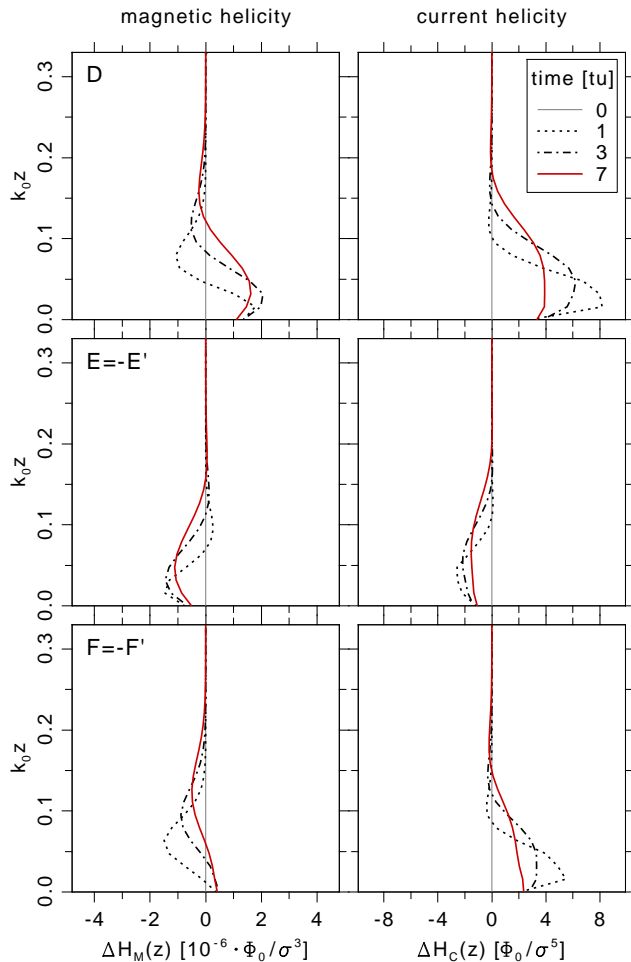


**Figure 3.** Similar to Figure 2, but for the four-spot configuration listed in Table 2.

ble 2, we compare the  $S$  values for all possible four-spot arrangements and find agreement with the signs and relative magnitudes of the actual magnetic helicity in the lower part of the domain. Values denoted with  $\uparrow$  are from the upper part of the domain, where both signs contribute significantly in Figure 3. We find that the sign changes of  $S$  correlate well with those of the generated helicities in the lower part of the domain. Also, the magnitude of  $S$  correlates with the strength of the generated helicities. When  $S$  is small, the correlation with the helicities is less clear. On the other hand, compared with the three-spot configurations, the correspondence with the actual signs of current helicity, and sometimes also the relative magnetic helicity, tends to be the other way around. The reason for this is not obvious, but the different trends for magnetic and current helicities suggest that this is connected with helicity effects from different length scales. Therefore, investigating helicity spectra will be an important future task.

### 2.6. Application to solar magnetograms

Nearly force-free magnetic field configurations have been generated in numerical simulations by several groups (Gudiksen & Nordlund 2002, 2005a,b; Bingert & Peter 2011; Bourdin et al. 2013) using observed solar magnetograms as lower initial and boundary conditions, where the vertical magnetic field was kept fixed. They showed that random footpoint motions lead to field line braiding

and coronal heating. Force-free magnetic fields are generally helical, but the initial potential field and the random footpoint motions were nonhelical, so no net sign of magnetic helicity was expected. This turned out not to be the case. Instead, these simulations produced net magnetic helicity, which Bourdin et al. (2018) used to study the vertical variation of the resulting magnetic and current helicity profiles and the possibility of a magnetic helicity reversal with height, as has been suggested from studies of magnetic helicity in the solar wind (Brandenburg et al. 2011) and theoretical studies (Warnecke et al. 2011, 2012). The point of the present work is to provide the theoretical underpinning to why a finite value of the magnetic helicity can be expected in these simulations that are otherwise statistically mirrorsymmetric. In fact, the coronal simulations of Rempel (2017) also have finite magnetic current helicity (M. Rempel 2018, private communication), but in their case this could also be a remnant from the initial magnetic field that was taken from a large-scale dynamo simulation.

The images of  $B_z$  for A and A' in Figure 1 can be identified with those of open left (L) or right (R) hands, respectively. Here, the palm corresponds to the biggest spot, the thumb points to the smallest one, and the four fingers to the intermediate spot. Their orientation indicates the expected sign of helicities, where left-handed regions should generate negative helicity and right-handed ones positive helicity. The polarity of the spots is of no importance for the sign of the generated, even though we find that mixed polarities generate more helicity.

Our work raises the possibility that magnetic helicity can be determined even from a magnetic field with a  $180^\circ$  ambiguity and, in particular, from the relative arrangement of sunspots on the solar surface. We have seen in Section 2.4 that helicity is also generated if all spots feature the same polarity, even though such setups create less helicity than multipolar ones. This suggests remarkable prospects for future work, whose full extent cannot be imagined at present, given that detailed sunspot observations exist for many centuries.

### 3. Conclusions

With the help of our model, we have demonstrated that magnetic helicity is generated above the surface of a star like the Sun and that its sign can be determined uniquely from the horizontal arrangement of magnetic flux concentrations and not just, as previously thought, by the twist of the emerging magnetic field. The source of this magnetic field is the solar dynamo, and it also determines the sign of magnetic helicity. This helicity manifests itself in a powerful way through the spot arrangement. We have demonstrated this by taking an observed solar magnetogram, removing all other signs of magnetic helicity by fitting it to a potential field, and then finding the original sign of magnetic helicity being recovered through the spot arrangement alone (Bourdin et al. 2018). This illustrates a strong persistence of magnetic helicity characterized by this new aspect of handedness.

An immediate implication of our work is that the horizontal arrangement of just the line-of-sight magnetic field or—more precisely—the vertical magnetic field, contributes to determining the sign of magnetic helicity in the region above. Such magnetograms have commonly been used in earlier studies of coronal heating. Although footpoint motions can lead to random twist of magnetic field lines, the

net effect vanishes, as has been confirmed in the simulations of Bourdin et al. (2013). Nevertheless, net magnetic helicity has been detected in those simulations; see Bourdin et al. (2018). Our present results now give us a theoretical framework with which this surprising fact can be understood. In the simulations of Bourdin et al. (2013), the underlying solar magnetogram was taken from a location on the southern hemisphere slightly below the solar equator. Thus, if any net magnetic helicity is to be expected, it should be positive (Seehafer 1990). This is indeed what is found in the simulations. This suggests that the sign of magnetic helicity must have been imprinted on the pattern of the emerged magnetic flux at the surface through its complex arrangement that cannot be modeled using only a pair of spots. Three or more spots or magnetic flux concentrations are needed to encode the information about magnetic helicity in the surface pattern.

Our work has future applications to solar physics and, perhaps, many other fields. Even just sunspot and starspot observations can in principle be used to gather information about magnetic helicity. Besides the original application of Tashiro et al. (2014) to extragalactic high-energy gamma rays, other possible applications in astrophysics may include galactic magnetism, where magnetic helicity was previously only accessible through Faraday rotation measurements (Oppermann et al. 2011; Brandenburg & Stepanov 2014). Other approaches are conceivable where the sign of magnetic helicity is in principle accessible through the measurement of what is known as E and B polarization (Seljak & Zaldarriaga 1997; Kamionkowski et al. 1997), i.e., the parity-even and parity-odd contributions to the linear polarization in the sky (Kahniashvili et al. 2014). The relation between this and our present work still needs to be elucidated in more detail.

We thank the anonymous referee for useful suggestions and the idea to associate the images of spot arrangements with the palm, fingers, and thumb of left and right hands. This work is financially supported by the Austrian Space Applications Programme at the Austrian Research Promotion Agency, FFG ASAP-12 SOPHIE under contract 853994. This research was supported in part by the NSF Astronomy and Astrophysics Grants Program (grant 1615100), and the University of Colorado through its support of the George Ellery Hale visiting faculty appointment. We acknowledge the allocation of computing resources provided by the Swedish National Allocations Committee at the Center for Parallel Computers at the Royal Institute of Technology in Stockholm. This work utilized the Janus supercomputer, which is supported by the National Science Foundation (award number CNS-0821794), the University of Colorado Boulder, the University of Colorado Denver, and the National Center for Atmospheric Research. The

Janus supercomputer is operated by the University of Colorado Boulder.

## References

- Berger, M. A., & Field, G. B. 1984, *J. Fluid Mech.*, **147**, 133–148
- Bingert, S., & Peter, H. 2011, *A&A*, **530**, A112
- Bourdin, P.-A., Bingert, S., & Peter, H. 2013, *A&A*, **555**, A123 (6pp)
- Bourdin, P.-A., Singh, N., & Brandenburg, A. 2018, *ApJ*, in print, arXiv:1804.04153
- Brandenburg, A. 2005, *ApJ*, **625**, 539–547
- Brandenburg, A., & Stepanov, R. 2014, *ApJ*, **786**, 91
- Brandenburg, A., & Subramanian, K. 2005, *Phys. Rep.*, **417**, 1–209
- Brandenburg, A., Subramanian, K., Balogh, A., & Goldstein, M. L. 2011, *ApJ*, **734**, 9
- Brandenburg, A., & Zweibel, E. G. 1994, *ApJL*, **427**, L91–L94
- Canfield, R. C., Hudson, H. S., & McKenzie, D. E. 1999, *Geophys. Res. Lett.*, **26**, 627–630
- Chen, F., Peter, H., Bingert, S., & Cheung, M. C. M. 2015, *Nat. Phys.*, **11**, 492–495
- Finn, J. M., & Antonsen, Jr., T. M. 1985, *Comments Plasma Phys. Controlled Fusion*, **9**
- Gibson, S. E., Fletcher, L., Del Zanna, G., et al. 2002, *ApJ*, **574**, 1021–1038
- Gudiksen, B., & Nordlund, Å. 2002, *ApJL*, **572**, L113–L116
- . 2005a, *ApJ*, **618**, 1020–1030
- . 2005b, *ApJ*, **618**, 1031–1038
- Kahniashvili, T., Maravin, Y., Lavrelashvili, G., & Kosowsky, A. 2014, *Phys. Rev. D*, **90**, 083004
- Kamionkowski, M., Kosowsky, A., & Stebbins, A. 1997, *Phys. Rev. Lett.*, **78**, 2058–2061
- Krause, F., & Rädler, K.-H. 1980, *Mean-field Magnetohydrodynamics and Dynamo Theory* (Oxford, Pergamon Press, Ltd.)
- Magara, T., & Longcope, D. W. 2001, *ApJL*, **559**, L55–L59
- Martin, S. F. 1998a, *Sol. Phys.*, **182**, 107–137
- Martin, S. F. 1998b, in *Astronomical Society of the Pacific Conference Series*, Vol. 150, IAU Colloq. 167: New Perspectives on Solar Prominences, ed. D. F. Webb, B. Schmieder, & D. M. Rust, **419**
- . 2003, *Adv. in Space Res.*, **32**, 1883–1893
- Oppermann, N., Janklewitz, H., Robbers, G., & Enßlin, T. A. 2011, *A&A*, **530**, A89
- Panasenco, O., Martin, S., Joshi, A. D., & Srivastava, N. 2011, *J. Atmos. & Sol.-Terr. Phys.*, **73**, 1129–1137
- Panasenco, O., & Martin, S. F. 2008, in *Astronomical Society of the Pacific Conference Series*, Vol. 383, *Subsurface and Atmospheric Influences on Solar Activity*, ed. R. Howe, R. W. Komm, K. S. Balasubramanian, & G. J. D. Petrie, **243**
- Panasenco, O., Martin, S. F., Velli, M., & Vourlidas, A. 2013, *Sol. Phys.*, **287**, 391–413
- Parker, E. N. 1979, *Cosmical magnetic fields: Their origin and their activity* (Oxford, Clarendon Press; New York, Oxford University Press), **858 pp**
- Rempel, M. 2017, *ApJ*, **834**, 10
- Seehafer, N. 1990, *Sol. Phys.*, **125**, 219–232
- Seljak, U., & Zaldarriaga, M. 1997, *Phys. Rev. Lett.*, **78**, 2054–2057
- Tashiro, H., Chen, W., Ferrer, F., & Vachaspati, T. 2014, *MNRAS*, **445**, L41–L45
- Tashiro, H., & Vachaspati, T. 2015, *MNRAS*, **448**, 299–306
- Valori, G., Kliem, B., & Fuhrmann, M. 2007, *Sol. Phys.*, **245**, 263–285
- Warnecke, J., Brandenburg, A., & Mitra, D. 2011, *A&A*, **534**, A11
- . 2012, *J. Space Weather & Space Clim.*, **2**, A11
- Yang, W. H., Sturrock, P. A., & Antiochos, S. K. 1986, *ApJ*, **309**, 383–391